

Strong Lensing Analysis of the Cluster RCS0224-0002 at $z = 0.77$

J. Rzepecki¹, M. Lombardi¹, P. Rosati¹, A. Bignamini², and P. Tozzi²

¹ European Southern Observatory, Karl-Schwarzschild-Strasse 2,85748 Garching bei Munich, Germany
e-mail: jrzepeck@eso.org

² INAF, Osservatorio Astronomico di Trieste, via G.B. Tiepolo 11, 34131, Trieste, Italy

ABSTRACT

Aims. We present a detailed mass reconstruction of the cluster RCS0224-0002 at $z = 0.773$ from the strong lensing features observed with HST/WFPC2.

Methods. The mass profile is reconstructed using a parametric approach. We introduce a novel method to fit extended multiple images based on the Modified Hausdorff Distance between observed arcs and the arcs reproduced by the model. We perform the detailed error analysis of the model parameter using the MCMC method.

Results. Our model reproduces all the observed strong lensing features of the RCS0224-0002 and predicts the redshift of one of the arcs systems to be $z \approx 2.65$ (the other system has a spectroscopic redshift of $z = 4.87$). The reconstructed inner mass profile is well fitted by a non-singular isothermal sphere, rather than with an NFW model. Dark matter substructure, derived from the light distribution of the most luminous cluster members, is crucial for reproducing the complexity of the quadrupole image system, which could not be achieved otherwise. The reconstructed mass distribution closely follows the light, however it is significantly shifted from the X-ray emission of the gas. The mass of RCS0224-0002 derived from the lensing model, $\approx 2 \times 10^{14} M_{\odot}$ is in a very good agreement with the one obtained from the X-ray temperature measured with deep Chandra observations.

Key words. Gravitational lensing – Galaxies: clusters: individual: RCS0224-0002

1. Introduction

The presence of dark matter is evident in galaxy clusters, where the mass to light ratios, $M/L \approx 200 h (M_{\odot}/L_{\odot})$, by far exceeds the mass of stars, and the hot gas implied by X-ray data (Hradecky et al. 2000). Gravitational lensing is one of the most attractive methods to directly study the mass distribution in the Universe on different scales, regardless of its component and dynamical state (see e.g. *ESA-ESO Working Groups, Report No. 3*, Peacock & Schneider 2006). Strong gravitational lensing in galaxy clusters leads to the formation of multiple images and giant luminous arcs (e.g. Schneider, P. and Ehlers J. and Falco E. 1992). Observations of these features allow us to investigate the distribution of the mass responsible for the deflection, and in particular provide accurate estimates of the *total* mass within giant arcs and the innermost density profile, which can be compared with N-body simulations. In addition, mass models can reveal the location of highly magnified background galaxies and allow spectroscopic studies of very distant faint, highly magnified sources, that would be under normal circumstances beyond the reach of 10m-class telescopes.

Accurate estimates of the mass profiles of galaxy clusters are fundamental for the modern cosmology since they provide severe tests for the theories of structure formation. The most popular theory based on the assumption of non interacting cold dark matter predicts a universal profile (NFW, Navarro et al. 1996) rather than an isothermal profile. For the lensing cluster Abell 1689, Broadhurst et al.

(2005a) ruled out the isothermal profile with 10σ confidence. However, another study of the same cluster by Halkola et al. (2006) shows that both the elliptical NFW and the isothermal softened elliptical fit the data well. Hence, although deep observations of this cluster showed a formidable arc system, *parametric* strong lensing models surprisingly lead to different mass density profiles, highlighting the difficulty of current inversion techniques in determining the uniqueness of the solution and the real uncertainties of the reconstructed mass maps

Here we present a study of the cluster RCS0224-0002 at $z = 0.773$ which was discovered as a part of the Red-Sequence Cluster Survey (RCS, Gladders et al. 2002). After the identification of the main strong lensing features of this cluster with VLT spectroscopy, follow-up observations were carried out with HST-WFPC2 by Gladders et al. (2002), in X-rays with the Chandra observatory (Hicks et al. 2005), and in sub-mm using SCUBA on the JCMT (Webb et al. 2005).

We construct a parametric model of the projected mass density distribution of RCS0224-0002 based on its strong lensing features, one of which with secure redshift. The method used in this paper to construct the best mass model is based on the so-called Modified Hausdorff Distance (MHD, Dubuisson & Jain 1994), and has the advantage of allowing us to use the information provided by the sub-arcsecond morphology of arcs. We compare the mass distribution with the spatial distribution of the hot gas obtained from the X-ray data.

When we were finalizing this paper, a lensing model of the same cluster has been independently presented by

Swinbank et al. (2007). However, these authors focus their work on the properties of a highly magnified $z = 4.87$ galaxy observed in the field; moreover, their lensing model, which is based only on the constraints provided by a single arc system (the giant arc labeled A in Fig. 1), is significantly different from ours.

The paper is structured as follows: In Sect. 2 we present data available on the RCS0224-0002. In Sect. 3 we discuss the strong lensing features and the red sequence of the RCS0224-0002. Section 4 is dedicated to the X-ray emission of the RCS0224-0002. In Sect. 5 we present assumptions behind our model and the method we use to obtain the projected mass distribution. In Sect. 6 we present and discuss our results. In Sect. 7 we perform error estimation. And finally in Sect. 8 we present our conclusions.

In this paper we use a standard cosmological model with $\Omega_m = 0.3$, $\Omega_\Lambda = 0.7$, and $H_0 = 72 \text{ km s}^{-1} \text{ Mpc}^{-1}$. We give all the magnitudes in the AB system, if not otherwise specified.

2. Observations

The HST observations of the RCS0224-0002 were taken on the 2001/08/20 in two filters, F606W and F814W using the WFPC2 camera (PI: Gladders, Proposal ID: 9135). The target coordinates were RA: 02:24:30.82, DEC: $-00:02:27.8$ and the exposure time for each filter was 1100 seconds. The WFPC2 data reduction was performed by Associations Science Products Pipeline.¹

The X-ray data were taken on the 2002/11/15 with the ACIS-S instrument on the Chandra observatory (PI: Gladders, Proposal Num: 03800013). The target coordinates were RA: 02:24:34.10, DEC: $-00:02:30.90$ and the exposure time was 14560 seconds. On the 2004/12/09, RCS0224-0002 was observed with the ACIS-S again (PI: Ellingson, Proposal ID: 05800899) with exposure time of 90150 seconds. The two ACIS-S observations were combined with CIAO 3.3, using CALDB 3.2.1, leading to 100.8 ksec of effective exposure time. Details on the reduction and spectral analysis, whose results are given below, can be found in Balestra et al. (2007).

3. Arc identification and cluster members

RCS0224-0002 has seven prominent luminous arcs and arclets marked as A1, A2, A3, B1, B2, B3, and B4 in Fig. 1. Unfortunately, out of those seven arcs, only one arc system (A) has a confirmed spectroscopic redshift of 4.87 (Gladders et al. 2002). The same authors estimated the redshift of system B within the range 1.4 to 2.7 based on the lack of emission lines in their spectra. Since the redshifts of arcs B1, B2, B3, and B4 are not known, an assumption needs to be made of whether all those arcs are images of one source or more sources. Based on very similar color, structure and distance from the center of the cluster we suppose that arcs B1, B2, B3, and B4 are images of one source and we call it system B. This conjecture is supported by the lensing model described below, since by assuming the existence of two separate systems (B1–B2, B3–B4) our model predicts relatively bright multiple images which are not observed. We excluded that the feature D is a radial arc, despite its elongated morphology, since no tangential counter

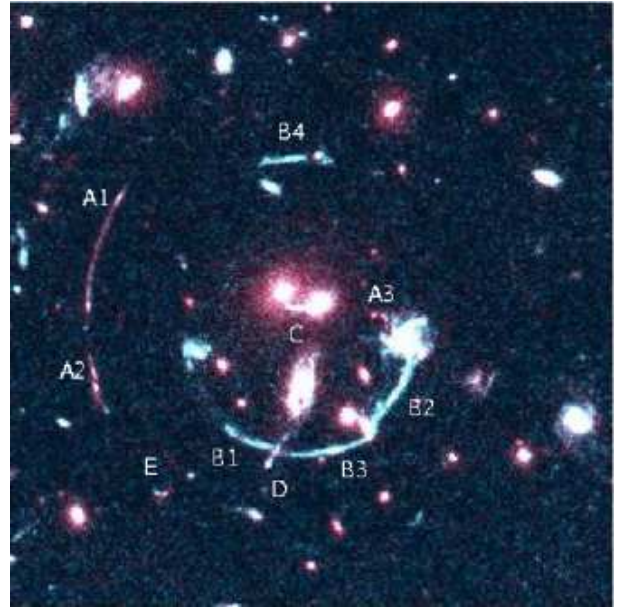


Fig. 1. The RCS0224-0002 cluster with labeled arcs. Color image composed from F814W and F606W WFPC2 HST images. The image is 40 arcsec across.

images are visible and because its position and morphology makes this hypothesis unlikely. Our model suggests that feature C is a central demagnified image, which is clearly visible in Fig. 4 showing the F606W image after subtracting the two cD galaxies. There is also a very faint arc, labeled E, which was not included in our analysis.

Since mass is known to follow light in galaxy clusters (see e.g. Sand et al. 2002), the distribution of color selected cluster members is often used to model substructure of the underlying dark matter. Besides to the two brightest central galaxies (BCGs), there is no public spectroscopic information available in the field, we then used the red sequence to identify likely cluster members. In Fig. 2 we show the color-magnitude diagram over the whole WFPC2 field, highlighting red sequence objects lying within $15''$ from the cluster core. Photometry was performed using SExtractor software (Bertin & Arnouts 1996), by detecting sources in the F814W band and measuring $F606W - F814W$ colors with aperture of $1''$ diameter². The solid and dot-dashed lines represent our best fit to the red sequence and the best fit found by Best et al. (2002) for the cluster MS1054 at $z = 0.83$ for the same filters, after applying a K-correction of 0.07 mag. Red sequence objects were defined as those within ± 0.25 mag of the best fit line.

4. X-ray emission

The X-ray emission traces the hot gas trapped in the cluster potential well. The gas itself contributes about 15% to the total mass of the cluster and for relaxed systems traces closely the total mass density distribution. We overlay the X-ray contours of RCS0224-0002 from the 100 ksec Chandra observations in the 0.5–2 keV band onto the WFPC2 image in Fig. 5. The overall X-ray emission is

² The WFPC2 zero points were calculated according to: $ZP_{AB} = -2.5 \log(PHOTFLEM) - 21.1 - 5 \log(PHOTPLAM) + 18.6921$

¹ http://archive.eso.org/archive/hst/wfpc2_asn/wfpc2_products.htm

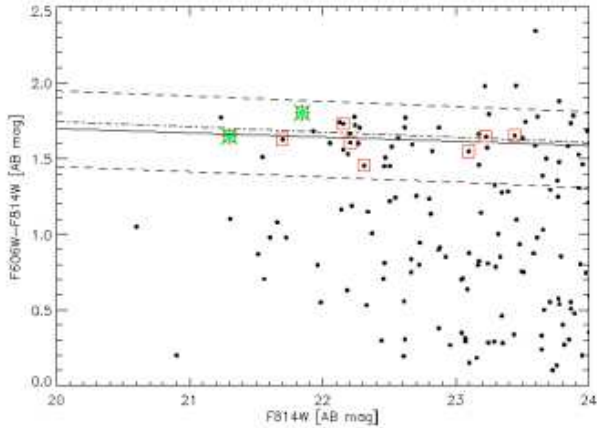


Fig. 2. The color-magnitude diagram of RCS0224 with the WFPC2 F606W/F814W filters. The dots represent all objects in the field. The squares represent the cluster red sequence (galaxies within 15 arcsec from the cluster center), the stars mark two central galaxies. The solid and dot-dashed lines are our best fit to the red sequence and the one of MS1054 at similar redshift.

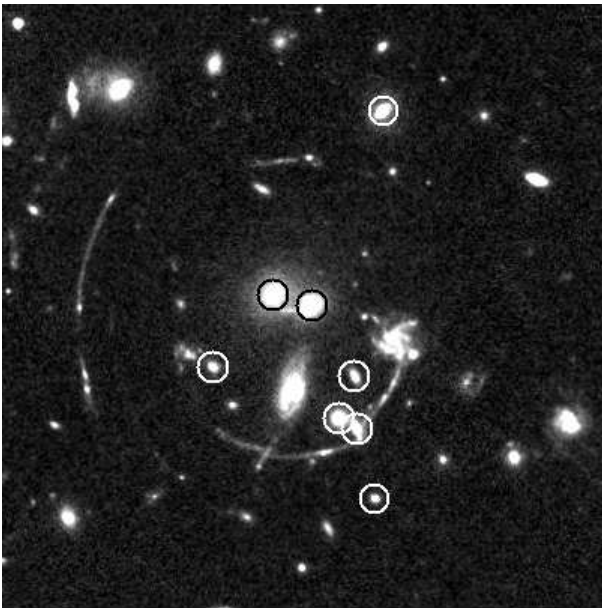


Fig. 3. The red sequence galaxies visible on the F814W filter WFPC2 HST image (objects that are marked here correspond to the squares in Fig 2).

not symmetric, with a plume extending NW, and its peak shifted ~ 5 arc seconds north from the two central BCGs. To measure the X-ray temperature, we used and extraction region of 36.7 arcsec (or 265 kpc), which encompasses most of the X-ray emission by maximizing the signal-to-noise. The background subtracted, unfolded spectrum is shown in Fig. 6. We used Xspec v.12.3.0 Arnaud (1996) to fit the data with a single temperature Mekal model (Kaastra 1992; Liedahl et al. 1995) and model the Galactic absorption with tbabs (Wilms et al. 2000), fixing the Galactic neutral Hydrogen columns density to the Galactic value obtained with radio data (Dickey & Lockman 1990). Since the signal-to-noise ratio in each energy bin is low, we used the C-statistics for the best fit model, over the energy range 0.6-

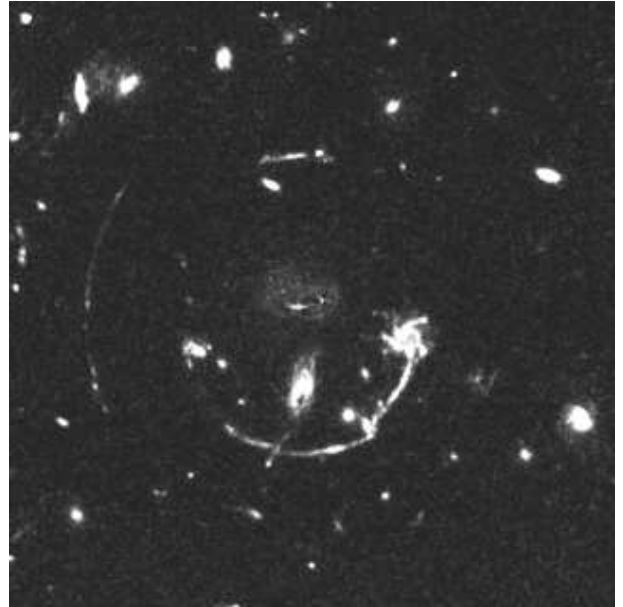


Fig. 4. RCS0224-0002 in the F606W filter with subtracted cD galaxies. The central radial feature C is clearly visible.

8.0 keV (excluding low energy photons due to uncertainties of ACIS calibration). We used 742 ± 35 total net counts in the fit (514 ± 23 in the soft 0.5-2 keV band) and found a best fit temperature of $kT = 5.26^{+1.14}_{-1.07}$ keV (1-sigma error). The de-absorbed flux within the extraction aperture, in the (0.5 - 2.0) keV band, is $1.84 \times 10^{-14} \text{ erg cm}^{-2} \text{ s}^{-1}$ and the rest-frame X-ray luminosity $L_X(0.5 - 2\text{keV}) = (0.38 \pm 0.02) \times 10^{44} \text{ erg s}^{-1}$. The bolometric luminosity returned by the best fit model is $L_{\text{BOL}} = (1.28 \pm 0.06) \times 10^{44}$. With these values of X-ray luminosity and temperature, we note that RCS0224-0002, which is an optically selected cluster, lies on the $L_X - T$ relation determined from large samples of X-ray selected clusters (e. g. Rosati et al. 2002)

We can use the measured cluster temperature to estimate the cluster mass assuming the hydrostatic equilibrium and isothermal distribution of the gas, with a polytropic index $\gamma = 1$. Using the standard β -model for the gas density profile, $\rho_{\text{gas}}(r) = \rho_0/[1 + (r/r_c)^2]^{3\beta/2}$, the mass within the radius r can be written as (Sarazin 1988):

$$M(< r) \simeq 1.11 \times 10^{14} \beta \gamma \frac{T(r)}{\text{keV}} \frac{r}{h^{-1}\text{Mpc}} \frac{(r/r_c)^2}{1 + (r/r_c)^2} h^{-1} M_{\odot}, \quad (1)$$

A fit to the X-ray surface brightness profile with the corresponding β -model $\text{SB}(r) \propto [1 + (r/r_c)^2]^{-3\beta+1/2}$ yields a core radius $r_c = (253 \pm 72) \text{ kpc}$ and $\beta = 0.97 \pm 0.3$. Therefore the mass within $R_{200} = 0.4 \text{ Mpc}$ is $(1.7 \pm 1.1) \times 10^{14} M_{\odot}$.

5. Model

We constructed the mass model of RCS0224-0002 by fitting the position and shapes of the multiple image systems A, B and C. Based on the light distribution of most luminous red-sequence galaxies, our model consists of several mass components: two isothermal non-singular ellipsoids to reproduce global cluster properties (NIE1, NIE2); eight isothermal non-singular spheres fixed at the position

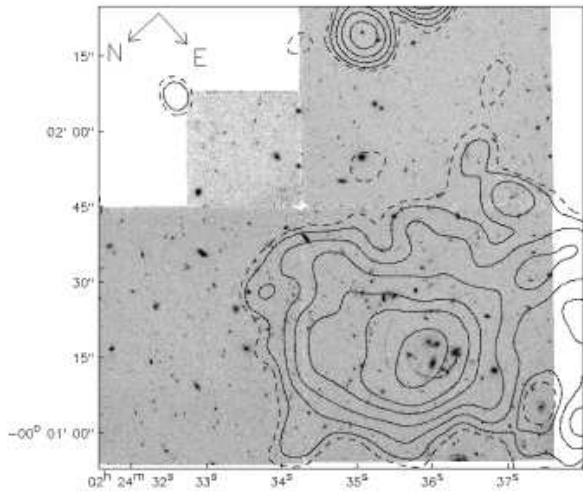


Fig. 5. The X-ray emission contours of RCS0224-0002 (smoothed with a Gaussian with $\sigma = 5''$) over-plotted on the F606W WFPC2 HST image.

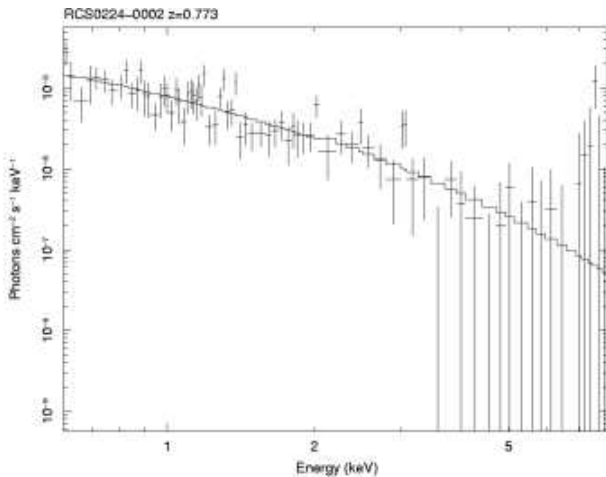


Fig. 6. X-ray spectrum of RCS0224-0002 from 100ksec Chandra observations, with the best fit Mekeal model, for $kT = 5.26^{+1.14}_{-1.07}$ keV.

of cluster members (NIS1.8) - referred to as the substructure; one non-singular ellipsoid, corresponding to the elongated object marked D in Fig. 1 (NIE3). In order to reduce the number of free parameters, we fixed the positions and the *relative* masses of the galaxy cluster clumps using the optical data available. In summary, we have 17 adjustable parameters in our model, including sources positions and unknown redshifts. All parameters are listed in Tables 1 and 2. The seven observed extended images are enough to constrain those 17 parameters due to the fact that we base our goodness of fit function not only on the position of the images but on the full information encoded in their shapes. Models including the radial feature D as a counter-image give the worst results, but as mentioned in Sect. 3, it is probably an foreground edge-on galaxy. Arc E was not used in the model since its redshift is unknown and it is too faint to provide any further constraint. We would like to empha-

size that we do not assign any physical meaning to the two distinct smooth components (NIE1&NIE2), and we are interested in the properties of the overall, combined profile. We have also tried to fit the data with only one smooth component (NIE1) and the substructure, however in that case we were not able to fit the arcs system B accurately.

5.1. Mass profiles

Although the N-body simulations of dark matter halo formation suggest NFW profiles rather than isothermal ones, recent strong lensing studies do not exclude and in some cases even prefer isothermal profile over NFW (Gavazzi et al. 2003; Halkola et al. 2006). We model here all mass components as non-singular isothermal ellipsoid, a simple generalization of a non-singular isothermal sphere often used as a physical representation of a gravitationally relaxed system. The use of isothermal profiles has also the advantage of being computationally less demanding. The associated gravitational potential ϕ , projected mass density ρ , and deflection angle α are given by

$$\phi(x_1, x_2) \equiv x_1 \frac{\partial \phi}{\partial x_1} + x_2 \frac{\partial \phi}{\partial x_2} \quad (2)$$

$$-bqs \ln [(\psi + s)^2 + (1 - q^2)x_1^2]^{1/2} + bqs \ln [(1 + q)s],$$

$$\alpha_1(x_1, x_2) \equiv \frac{\partial \phi}{\partial x_1} = \frac{bq}{\sqrt{1 - q^2}} \operatorname{atan} \left[\frac{\sqrt{1 - q^2}x_1}{\psi + s} \right], \quad (3)$$

$$\alpha_2(x_1, x_2) \equiv \frac{\partial \phi}{\partial x_2} = \frac{bq}{\sqrt{1 - q^2}} \operatorname{atanh} \left[\frac{\sqrt{1 - q^2}x_2}{\psi + q^2s} \right], \quad (4)$$

$$\psi^2(x_1, x_2) \equiv q^2(s^2 + x_1^2) + x_2^2, \quad (5)$$

$$\rho(x_1, x_2) \equiv \frac{1}{2} \frac{b}{(s^2 + x_1^2 + x_2^2/q^2)^{3/2}}, \quad (6)$$

where q is the ellipticity, s is the core radius, b is the scale factor and $\mathbf{x} = (x_1, x_2)$ is the position in the image plane. Note that the fast method for calculating the deflection angle of the softened non-singular ellipsoid might be found in Barkana (1998).

5.2. Minimization method

5.2.1. Source plane minimization

In order to get a first, approximated solution, we perform model fitting minimization on the source plane. This technique is computationally very efficient, since there is no need to solve the inverse problem of the lensing equation and the deflection angle is only computed at the position of the images. We also assume that sources are small compared to the scale of variations of the lensing potential. If we have N images at positions $\{\mathbf{x}_i\}$ corresponding to one source, then we define the χ^2 as

$$\chi_{\text{src}}^2 = \sum_i \delta \mathbf{u}_i^T \mu_i^T S_i^{-1} \mu_i \delta \mathbf{u}_i + P, \quad (7)$$

where

$$\delta \mathbf{u}_i = \mathbf{u}_{\text{obs},i} - \mathbf{u}_{\text{mod}}, \quad (8)$$

$$\mathbf{u}_{\text{obs},i} = \mathbf{x}_{\text{obs},i} - w \nabla \phi(\mathbf{x}_{\text{obs},i}). \quad (9)$$

In the previous equations, $\mathbf{u}_{\text{obs},i}$ is the source position (as predicted by the model) corresponding to the image $\mathbf{x}_{\text{obs},i}$, $\phi(\mathbf{x}_{\text{obs},i})$ is the lensing potential at image i , w is the cosmological weight of the source (see e.g. Lombardi & Bertin 1999), and μ_i is the magnification matrix (inverse of the Jacobian matrix of the lens mapping) at the image i . Moreover, in Eq. (7) we introduced the covariance matrix of the position measurements S . For simplicity, in this paper we assume that the covariance matrix is diagonal and takes the form

$$S_i = \begin{bmatrix} \sigma_i^2 & 0 \\ 0 & \sigma_i^2 \end{bmatrix} = \sigma_i^2 I, \quad (10)$$

where σ_i is estimated to be $\sim 0.05''$. In the definition of our χ^2 [Eq. (7)] we introduced also a “penalty” function P . This function, is used to bound some of the free parameters to certain intervals, and is chosen to have the functional form

$$P = \mathcal{P} \sum_{p=0}^N \text{atan}(10^7(b_{\text{down},i} - p_i)) + \text{atan}(10^7(p_i - b_{\text{up},i})) + \mathcal{P}\pi, \quad (11)$$

where, N is the number of bounded parameters in our model, p_i is the i -th bounded parameter, which is required to be in the range $[b_{\text{down},i}, b_{\text{up},i}]$. Note that the penalty function P behaves similarly to a “square potential well”, i.e. the sum of two Heaviside functions; however, the use of analytic functions ensures that P is differentiable and makes our minimization numerically stable. In order to effectively bound our parameters, we used a large number for the coefficient \mathcal{P} . When there is more than one source, the same procedure is repeated for all sources and the resulting χ^2 from Eq. (7) are added. The magnification matrix μ_i is included because $\mu_i \delta \mathbf{u}_i \approx \delta \mathbf{x}_i$, so that χ_{src}^2 is an approximation of χ^2 in the image plane. However, this also introduces a weight in the χ^2 term, as images for which $\mu_i \delta \mathbf{u}_i$ are small do not contribute significantly to the minimization process. It is possible to write an analytical expression for the source position that minimizes χ_{src}^2 :

$$\mathbf{u}_{\text{mod}} = A^{-1} \mathbf{b};, \quad (12)$$

$$A = \sum_i \mu_i^T S_i^{-1} \mu_i, \quad (13)$$

$$\mathbf{b} = \sum_i \mu_i^T S_i^{-1} \mu_i \mathbf{u}_{\text{obs},i}. \quad (14)$$

5.3. Extended images

The best fit model provided by Eq. (7) is used as starting point for the image plane analysis. This step is based on a new χ^2 minimization, with a χ^2 composed of two terms: the so-called Modified Hausdorff Distance (MHD, Dubuisson & Jain 1994) between the modeled and observed image sets and the “plain difference” between the same sets.

The MHD between two sets A and B is defined as

$$\text{MHD} = \max(h_{\text{ab}}, h_{\text{ba}}), \quad (15)$$

$$h_{\text{ab}} = \frac{1}{\|A\|} \sum_{a \in A} \min_{b \in B} \|a - b\|^2, \quad (16)$$

$$h_{\text{ba}} = \frac{1}{\|B\|} \sum_{b \in B} \min_{a \in A} \|a - b\|^2. \quad (17)$$

In addition, the “plain difference” between the observed and modeled arcs is computed as follows. All pixels in each observed arc system, generically called O , are assigned a value of 1; other pixels are assigned a value of -1 . The same procedure is applied to the corresponding modeled arcs (M) and the difference $\text{diff}(O, M) = |O - M|$ is calculated. In summary, the expression to minimize in the image plane is

$$X^2 = \text{MDH}(D, M) + \omega \text{diff}(M, D) + P. \quad (18)$$

The factor ω was chosen to be ~ 0.1 , since this value resulted in the fastest convergence. The penalty function P is used to bound some of the model parameters and it is defined in Sect. 5.2.1. By using two distance components, we ensure an efficient convergence of the minimization since when the modeled and the observed images start to overlap, the MHD becomes less sensitive to small variations than the plain difference. The *Powell* algorithm (Powell 1964) is used for all the minimization procedures.

6. Results

The best fit model (with MHD as defined by Eq. (15) equal to 30.3) is presented in Fig. 7. The values of corresponding parameters are given in Tables 1 and 2. The model reproduces fairly well all the observed strong lensing features. The giant arc A include a counter-image $7''$ to the west of the BCGs (A3). The model also reproduce the quadrupole system B (B1,..B4). The central feature C is also predicted fairly close to the observed one, although with different morphology. None of the models we analyzed could reproduce the radial feature D, which suggests that it is probably a foreground edge-on galaxy. In addition, inclusion of D to the lens model (NIE3) significantly improved our fits and allowed us to “break” the arcs system B into two arcs B1 and B3. The best fit redshift of the source for the system B is 2.65 ± 0.08 ; a spectroscopic redshift of these blue arcs, as well as object D, would provide a strong validation of our lensing model and could also be used to better constrain the mass distribution. Estimates of the statistical errors are discussed in the following section. Figure 8 and Tab. 3 show the results of some tests performed to assess how well the best fit model is able to reproduce the morphology of the multiple image systems A and B. For this purpose, we ray-trace a given image for each system (A2 and B1, marked with green boxes in Fig. 8) into the source plane by using its HST color image. This gives us the reconstructed source image. We then ray-trace back all the pixels from the source plane into the image plane, thus finding all counter-images of the given image. These reconstructed counter-images are finally compared with the observed ones (A1,3 and B2,3,4). In general, we find a good agreement, especially the knots in the A1 arc are very well reconstructed. The overall shapes of all the arcs in the system B are also accurately predicted. The mass of the cluster within $R_{200} = 0.4\text{Mpc}$ obtained

from the model is $1.9 \pm 0.1 \times 10^{14} M_{\odot}$ and its distribution is shown in Fig. 9. This is in a good agreement with an mass derived above from the X-ray temperature. Since we do not know all the cluster member galaxies, we cannot reliably estimate the mass-to-light ratio of the whole cluster. For the substructure (the mass associated with the luminous cluster component - NIS1..8), we find an average mass-to-light ratio $M/L_{B,vega} \approx 3.6 M_{\odot}/L_{\odot,B}$. We converted the observed F814W filter flux to the rest frame B filter flux, by calculating a k-correction for a template elliptical galaxy from Kinney et al. (1996). The center of the mass of the best fit model follows the light distribution. NIE1 is found to be a diffuse (core radius $\approx 15''$) mass component close to the peak of the X-ray emission. The latter is shifted $\approx 5''$ from the NIE2 component, which corresponds to the center of the potential well and the position of the BCGs. This may indicate the presence of a merger. The radial average profile of the best fit surface mass density is shown in Fig. 10. This can be well approximated by a power law profile with a slope $\gamma = 0.74^{+0.03}_{-0.04}$, which is closer to the isothermal profile ($\gamma = 1$) than results obtained in other clusters. For example, the analysis of the cluster J1004-4112 yielded $\gamma \approx 0.5$ (Sharon et al. 2005) and $0.3 < \gamma < 0.5$ (Williams & Saha 2004), whereas Broadhurst et al. (2005a) found $\gamma = 0.5$ in A1689 using a large number of identified multiple images. Note that the flat core of the mass profile we have found, being a result of a high value of the r_c of the NIE1 component, is well constrained by the position of the central arc C. The change of the r_c by 50% causes the shift in the C arc position of ≈ 1 arc sec.

By approximating the mass density distribution with NFW-like profile of the form

$$\rho(r) = \frac{\rho_0}{(r/r_c)^{\beta}(1+r/r_c)^{(1-\beta)}}, \quad (19)$$

we find a slope $0.69^{+0.09}_{-0.13}$, flatter than the canonical NFW model ($\beta = 1$), however in good agreement with other studies which obtained $\beta < 1$. For example, Sand et al. (2002) finds $\beta = 0.35$ for the galaxy cluster MS1237-23, and $\beta < 0.57$ (at 99% confidence level) from the analysis of a large sample of clusters (Sand et al. 2004).

In addition, we have tried to fit a model based the universal NFW profile rather than NIE. The result, presented in the Fig. 11, shows that an NFW model performs significantly worse than the NIE one. The arcs A1 and A2 are reproduced fairly well, but the counter image A3 is found much too far from the cluster center. In addition, in the NFW model feature B4 is split into two arcs (the second of which is not observed) and the reproduced arc B2 is shifted with respect to the observed one. This is reflected by the value of MHD, which is ten times bigger than the corresponding value for the best-fit NIE model. We note, however, that this bad performance might be due to the approximated NFW elliptical model used in our code, where the ellipticity is achieved by perturbing the potential of the spherical NFW profile instead of its density. This approximation holds for potentials close to spherical, and therefore we need to impose additional restrictions on the ellipticity of the NFW components.

7. Error analysis

Our method involves the minimization of the MHD whose expression (Eq.18) is not a formal χ^2 and includes a number of penalty functions (weights) to limit the range of some parameters. As a result, it is difficult to obtain reliable errors on the best fit parameters. In the presence of many parameters, the Monte Carlo Markov Chain (MCMC, see for example Neal 1993) method is an efficient way to estimate the likelihood associated to our best fit model. MCMC is used as a third step of our minimization process by reconstructing the probability distribution function of our model parameters. We start the construction of Markov chain using the *Metropolis* algorithm (Metropolis et al. 1953) from the best fit solution of the MHD minimization. We use a number of chains randomly distributed around the best fit point. The resulting chain being the composition of all those partial chains provides an approximate probability distribution function for our parameters, from which we estimate the confidence levels shown in the Fig. 12. Also by randomly probing the parameters space, the MCMC algorithm helps to fine tune our best fit parameters returned by the previous step of minimization. Most of the parameters are well constrained (within 10 - 20 percent). The unknown redshift of the arc system B appears to be well constrained, $z_B = 2.65 \pm 0.08$. The mass to light ratio of the substructure is however poorly constrained to be $3.6^{+3.3}_{-1.8}$.

We estimated the errors of a single power law and NFW-like profile parameters by drawing a random sample of models from our Markov Chain, and then fitting a single power law and NFW-like profile to that sample. The resulting error estimates are presented in Fig. 13. This shows that isothermal and NFW profiles are excluded with 99% confidence level.

8. Conclusions

We have performed a strong lensing analysis of the cluster RCS0224-0002 using HST/WFPC2 images in F814W and F606W bands. We used two arc systems: a red giant tangential arc $14''$ from the center, with measured redshift of 4.87, for which we identified an inner counter image, and a system of blue arcs at smaller radii with no spectroscopic information.

We have modeled the mass distribution with three mass components: isothermal spheres associated with the most luminous cluster members to model the substructure, and two isothermal ellipsoids to model the underlying smooth mass component. Since spectroscopic information is available in the literature only for two cD galaxies, we identified likely member galaxies in the cluster core from the red sequence, which is clearly detected in the F606W-F814W color distribution. To infer the mass distribution from the position and shapes of the strong lensing features we used a three-step approach: i) minimization of the size of the two sources on the source plane, ii) minimization of the difference between the observed and modeled arcs on the image plane, based on the Modified Hausdorff Distance, and iii) a refined estimate of the best fit parameters and errors analysis with the Monte Carlo Markov Chain. The resulting mass density reproduces all the strong features fairly well. The redshift of the blue arc system is predicted to be 2.65 ± 0.08 .

We find that the substructure made of nine isothermal components centered on the brightest cluster members, with $M/L_{B,vega} \approx 3.6M_{\odot}/L_{\odot,B}$ is crucial to exactly reproduce the shapes and positions of all the arcs.

By fitting a single power-law or NFW-like halo to the radial average mass density distribution we have found that both profiles are far from canonical isothermal and standard NFW: we have found the power-law parameter γ to be $0.74^{+0.03}_{-0.04}$ ($\gamma = 1$ for an isothermal profile) and steepness parameter for NFW-like profile β to be $0.69^{+0.09}_{-0.13}$ ($\beta = 1$ for a NFW profile), with the upper boundary very well constrained. Both those values are consistent with the results obtained by studying the strong lensing properties of other clusters (see Sand et al. 2002, 2004). The best fit NIS has $\sigma_v = 925$ km/s and $r_c = 11$ kpc; the best fit NFW has $R_{200} = 0.4$ Mpc and concentration parameter $c = 3.4^{+0.4}_{-0.5}$, similarly to other massive clusters ($c \approx 4$ for a $z = 0.18$ cluster Halkola et al. 2006, $c \approx 5$ for $z = 0.68$ cluster Williams & Saha 2004). However, a wide range of concentration parameters are found (e.g. for $c > 10$ see Broadhurst et al. 2005b). We have measured the total mass of the cluster within R_{200} to be $1.9 \pm 0.1 \times 10^{14} M_{\odot}$ and its main component may be well described by a two NISs with a $\sigma_{v1} = 945^{+30}_{-23}$ km/s, a $r_{c1} = 112^{+13}_{-14}$ kpc, a $\sigma_{v2} = 702^{+31}_{-28}$ km/s, and a $r_{c2} = 12^{+4}_{-2}$ kpc. The mass of RCS0224-0002 derived from the lensing model is in a very good agreement with the one obtained from the X-ray temperature measured with deep Chandra observations ($M_{200} = (1.7 \pm 1.1) \times 10^{14} M_{\odot}$).

This analysis shows that even with a limited number of identified multiple images we could constrain the mass distribution fairly accurately. This was possible, in the case of RCS0224-0002, because the two arcs systems are at very different angular diameter distances and probe significant fraction ($\approx 20\%$ for the arcs system A, and $\approx 60\%$ for the system B) of the Einstein rings. Further spectroscopic observations of the system B, as well as cluster members, will allow a very robust constraint of the mass density profile of the inner core of this cluster and its substructure.

Acknowledgements. We would like to thank Matthias Bartelmann for very useful discussions and comments, specifically on the usage of the MCMC method to estimate the errors of our model.

References

Arnaud, K. A. 1996, in ASP Conf. Ser. 101: Astronomical Data Analysis Software and Systems V, ed. G. H. Jacoby & J. Barnes, 17–+

Balestra, I., Tozzi, P., Ettori, S., et al. 2007, A&A, 462, 429

Barkana, R. 1998, ApJ, 502, 531

Bertin, E. & Arnouts, S. 1996, A&AS, 117, 393

Best, P. N., van Dokkum, P. G., Franx, M., & Röttgering, H. J. A. 2002, MNRAS, 330, 17

Broadhurst, T., Benítez, N., Coe, D., et al. 2005a, ApJ, 621, 53

Broadhurst, T., Takada, M., Umetsu, K., et al. 2005b, ApJ, 619, L143

Dickey, J. M. & Lockman, F. J. 1990, ARA&A, 28, 215

Dubuisson, M. P. & Jain, A. K. 1994, ICPR, A:566

Gavazzi, R., Fort, B., Mellier, Y., Pelló, R., & Dantel-Fort, M. 2003, A&A, 403, 11

Gladders, M. D., Yee, H. K. C., & Ellingson, E. 2002, AJ, 123, 1

Halkola, A., Seitz, S., & Pannella, M. 2006, MNRAS, 372, 1425

Hicks, A. K., Ellingson, E., Bautz, M., et al. 2005, Advances in Space Research, 36, 706

Hradecky, V., Jones, C., Donnelly, R. H., et al. 2000, ApJ, 543, 521

Kaastra, J. S. 1992, in Frontiers Science Series, ed. Y. Tanaka & K. Koyama, 533–+

Kinney, A. L., Calzetti, D., Bohlin, R. C., et al. 1996, ApJ, 467, 38

Liedahl, D. A., Osterheld, A. L., & Goldstein, W. H. 1995, ApJ, 438, L115

Lombardi, M. & Bertin, G. 1999, A&A, 342, 337

Metropolis, N., Rosenbluth, A. W., Rosenbluth, M. N., Teller, A. H., & Teller, E. 1953, Journal of Chemical Physics, 21(6), 1087

Navarro, J. F., Frenk, C. S., & White, S. D. M. 1996, ApJ, 462, 563

Neal, R. M. 1993

Peacock, J. & Schneider, P. 2006, ESA-ESO Working Groups, Report No. 3

Powell, M. J. D. 1964, Computer Journal, 7, 152

Rosati, P., Borgani, S., & Norman, C. 2002, ARA&A, 40, 539

Sand, D. J., Treu, T., & Ellis, R. S. 2002, in Bulletin of the American Astronomical Society, 1208–+

Sand, D. J., Treu, T., Smith, G. P., & Ellis, R. S. 2004, ApJ, 604, 88

Sarazin, C. 1988, X-Ray Emission from Clusters of Galaxies (Cambridge: Cambridge Univ. Press)

Schneider, P. and Ehlers J. and Falco E. 1992, Gravitational Lenses

Sharon, K., Ofek, E. O., Smith, G. P., et al. 2005, ApJ, 629, L73

Swinbank, A. M., Bower, R. G., Smith, G. P., et al. 2007, astro-ph/0701221v1

Webb, T. M. A., Yee, H. K. C., Ivison, R. J., et al. 2005, ApJ, 631, 187

Williams, L. L. R. & Saha, P. 2004, AJ, 128, 2631

Wilms, J., Allen, A., & McCray, R. 2000, ApJ, 542, 914

Table 1. Parameters defining our model (see equation 2–4) after minimization. Parameters in parenthesis were allowed to change during minimization

	NIE1	NIE2	NIS1	NIS2	NIS3	NIS4	NIE3	NIS5	NIS6	NIS7	NIS8
x_1	(16.834)	19.413	18.039	20.578	24.799	23.494	17.621	22.389	23.614	25.296	14.097
x_2	(18.502)	20.307	20.834	20.147	7.336	15.330	10.253	12.612	12.005	32.969	16.076
z	0.782	0.782	0.782	0.782	0.782	0.782	0.782	0.782	0.782	0.782	0.782
b	(19.196)	(10.086)	(0.116)*	(0.191)*	(0.027)*	(0.032)*	(0.417)	(0.081)*	(0.075)*	(0.087)*	(0.037)*
q	(0.396)	(0.597)					0.3				
θ	(2.994)	(1.409)					0.873				
s	(15.539)	(1.778)	0.1	0.1	0.1	0.1	0.1	0.1	0.1	0.1	0.1

x_1, x_2 : central position in arc seconds in the coordinate system of the Fig. 9, z : redshift, b : scale factor in arc seconds, q : ellipticity, θ : position angle in radians, s : core radius in arc seconds


















* – for the substructure the M/L ratio has been used as the variable for the minimization

Table 2. Parameters defining sources after minimization. Parameters in parenthesis were allowed to change during minimization

	SOURCE1	SOURCE2
u_1	(15.979)	(18.892)
u_2	(19.204)	(19.412)
z	4.878	(2.648)

U_1, U_2 : source position in arc seconds, z : redshift

Table 3. Images reproduced under image plane – source plane – image plane mapping

Image	Counter Images Reproduced Images		
A2 	A1  A3 		
			x2
			x2
B1 	B2  B3  B4 		
			
			

First column shows images used to construct sources. Second column shows both original and model reproduced images.

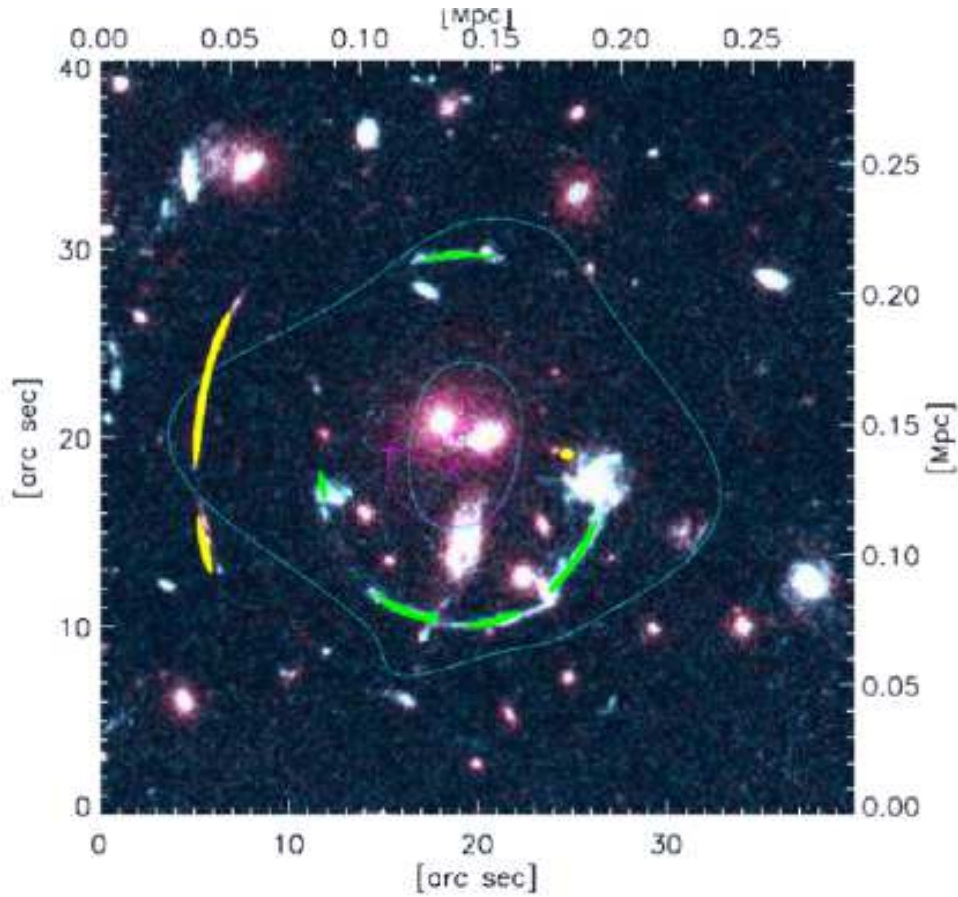


Fig. 7. Images reproduced by our best fit model over-plotted on the combined F606W/F814W WFPC2 HST image. The closed lines show the critical curves and caustics for a source at $z = 4.87$. The center of the image is at RA 02:24:34.218, Dec -00:02:31.64.

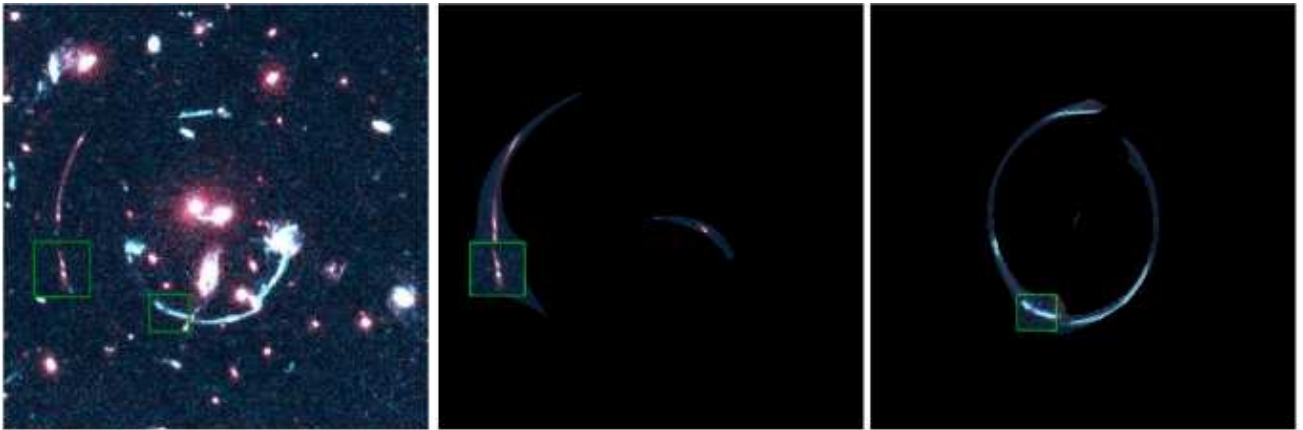


Fig. 8. Result of image plane – source plane – image plane mapping. Panel to the left shows the arcs (marked by boxes) used to reproduce the arc systems. Middle and right panels show the arc systems as reproduced by the best fit mass model (the box marks the original image).

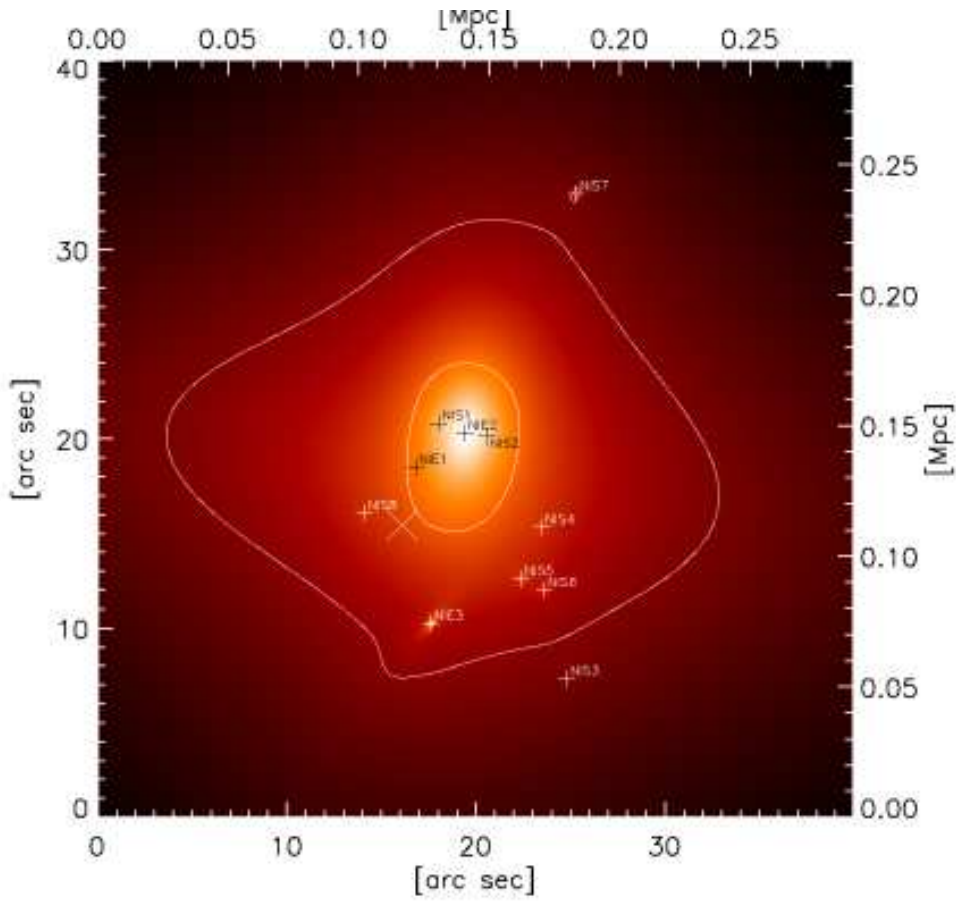


Fig. 9. Mass density produced by our best fit model. The closed lines are the critical curves for a source at $z = 4.87$. The crosses (+) mark the positions of our model components. The big cross (X) gives the position of the peak of the X-ray emission. The center of the image is at RA: 02:24:34.218 Dec: -00:02:31.64, the orientation as in Fig. 5

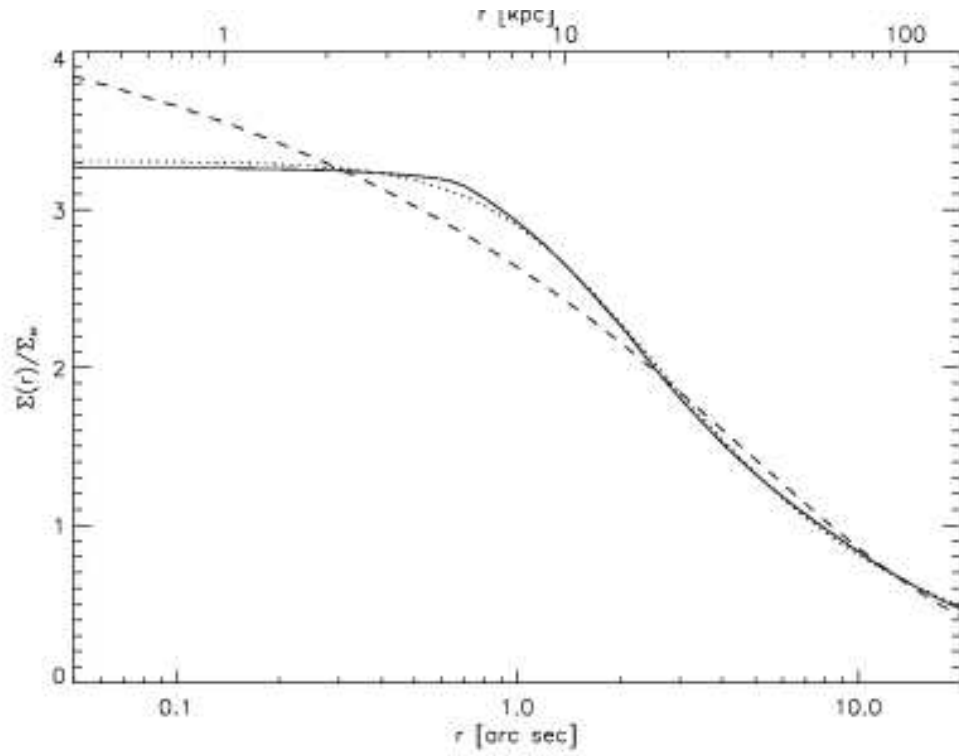


Fig. 10. Radial average profile of the surface mass density of our best fit model (solid line) versus power law profile with $\gamma = 0.74$ (dotted line) and NFW-like profile with $\beta = 0.69$ (dashed line).

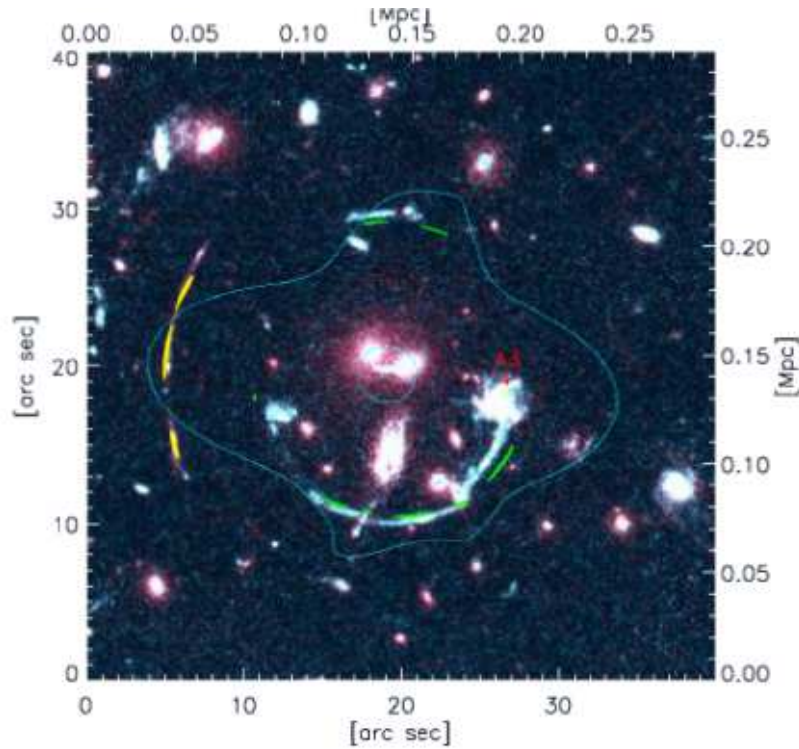


Fig. 11. Images reproduced by our best fit NFW model over-plotted on the combined F606W/F814W WFPC2 HST image. The closed lines are the critical curves for a source at $z = 4.87$. The center of the image is RA: 02:24:34.218 Dec: -00:02:31.64

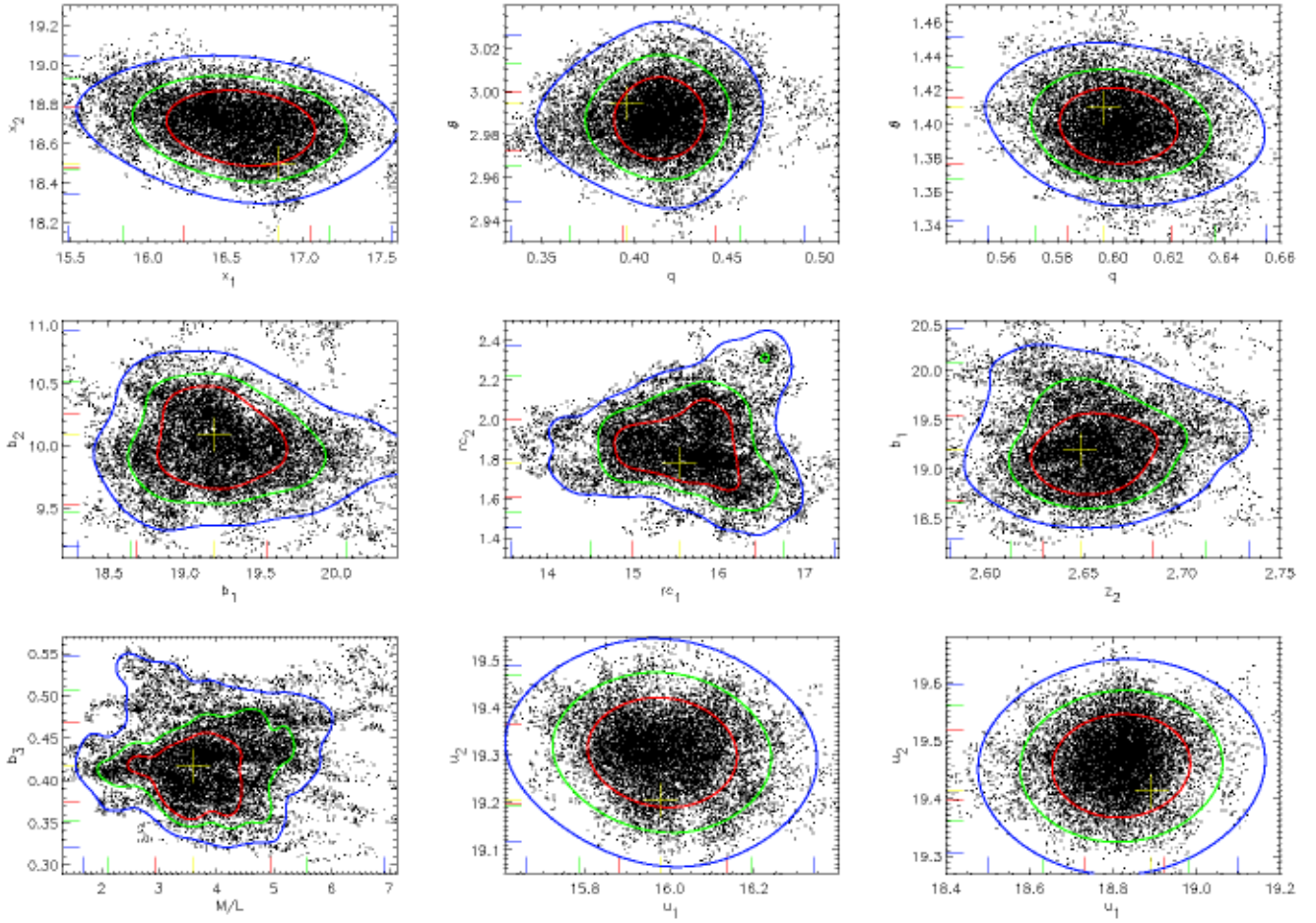


Fig. 12. MCMC error estimates. The contours correspond to 68%, 90% and 99% confidence levels. Marks on vertical and horizontal axis give the same confidence levels for 1D projected variables. The cross marks the position of the best fit point.

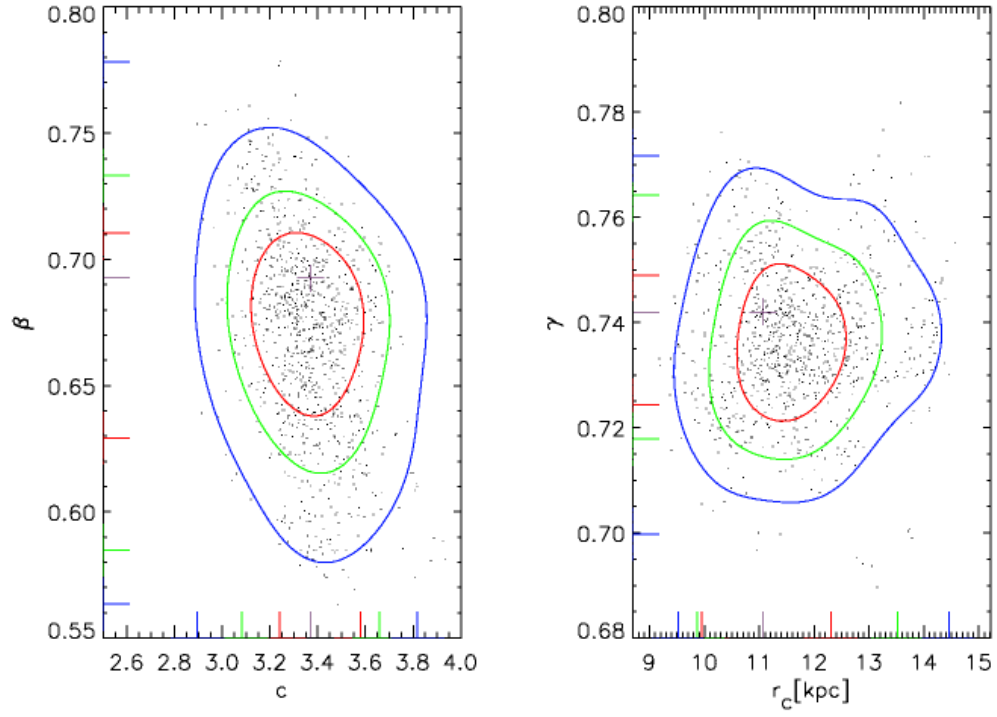


Fig. 13. MCMC error estimates of the parameters of the single power law and NFW-like profiles fit. The contours correspond to 68%, 90% and 99% confidence levels. Marks on vertical and horizontal axis give the same confidence levels for 1D projected variables. The cross marks the position of the best fit point.